3E03

Can gas phase calculations be effective in generating the novel chemistry of organic-inorganic halide perovskite solar cells?

(Department of Chemical System Engineering, School of Engineering, The University of Tokyo, 7-3-1 Hongo, Bunkyo-ku, Japan 113-8656)

[O] Pradeep R. Varadwaj, Arpita Varadwaj, Koichi Yamashita

E-mail: pradeep@tcl.t.u-tokyo.ac.jp

[**Introduction**] The organic-inorganic methylammonium lead(/tin/germanium) halide hybrid perovskites, symbolically MAPb(/Sn/Ge)X_3 (X = Cl, Br, I), are a specific class of mineral based novel photocatalytic systems. They are magically so feverish and so natural that they have gone viral in solar sector today to advance scientific research in future energy technology.[1] An underlying reason for which they are considered as most crucial lies in their technological adamant in the solar technology race since they can take the sunlight in and generate the electricity out similar to any novel photo-catalyst.[2,3] The perovskites fall in the class of low band gap materials such that their band gap in the 1.5–3.1 eV can be tunable changing the halogen and metal contents.[2] Another reason for which scientists put too much emphasis on these lies in their unique chemico-physical, electrical, optoelectronic, and materials properties that are least understood, needing further exploration covering areas as diverse as, *inter alia*, chemistry, physics, electrical, electronic synthetic and chemical engineering, crystallography, and in materials science and nanotechnologies.[3] The importance of these highly-valued materials can be realized by surveying the Web of science database. For instance, searching the simple keyword "*lead halide perovskite*" displays about 1200 peer reviewed publications catalogued in the literature. Our survey is consistent with Manser et al. [4a)] who have claimed a dramatic rise in the number of PSC-related publications to be more than 1100 from just a single primary article appeared in 2009 (the first one?), which are accompanied with 28000 indexed citations in 2015.

Researchers classify the MAPb(/Sn/Ge)X_3 perovskites as third-generation photovoltaic solar cell materials.[5] Their extraordinary device-based photon conversion performances gleaned within last five years have recently enforced Stoumpous et al. to refer these materials, as well as some of their mixed halogen derivatives $CH_3NH_3Pb(/Sn/Ge)(X_yI_{3-y})_{y=0-3}$(X=Cl, Br), to as a class of the poor man's high performance semiconductors,[6a)] even though they are not set ready for outdoor activities. An important reason for which these systems are put at the first place lies in their elemental constituents that are abundant, and cost-effective. They are also technologically advantageous over other known solar cells, e.g., silicon solar cells, GaAs, and CdSe, and organic solar cells, etc. These materials are easy-to-synthesize even in traditional/ordinary research laboratories, and are easily processable in solution. Because of these latter features they are competitive with the dye-sensitized solar cells, as well as with organic photovoltaic solar cells, in terms of device fabrication, and processing, etc.[4]

Sum and Park have realized that despite the expeditious research progress on halide perovskite solar cells, a comprehensible understanding of their fundamental and device-based sciences, e.g. interfacial charge dynamics, and origins of the current-voltage hysteresis, etc., is still lacking.[6b)] Therefore, attentive involvements of interdisciplinary groups of researchers with diverse scientific backgrounds are needed to address the nontrivial issues.

We are basically interested in part in the enhancement of the current understanding of the coordination and noncovalent chemistry, the origins of ferroelectricity, and the environmental instabilities, etc., of the halide perovskite materials. This is so as unambiguous and profound knowledges on these fundamental themes are essentially important in the strategic and controllable designs of novel materials of such kind.

In this presentation, we focus to discuss the density functional theory gas phase results of the structural, energetic, one-electron, charge density topological, and molecular orbital features (i) of the neutral clusters of lead trihalide anion (PbX_3^-) with methylammonium organic cation ($CH_3NH_3^+$), (ii) of the cationic and neutral clusters of the PbX_6^{4-} octahedral species with the organic cation, in which, each face of the octahedron occupies with one unit of the organic cation upon successive addition (same as in Fig. 1), and (iii) of the cationic clusters of $[(CH_3NH_3)_8PbX_6]^{4+}$ with water (H_2O) molecule(s). For the latter case, the number of H_2O molecules range from one up to ten. The coordination and physical chemistry of the above-mentioned clusters, especially the latter ones, are expected to have strong relevance with those of the $[(CH_3NH_3)_4PbI_6\bullet(H_2O)_{n=1,2}]$ zero-dimensional (0D) quantum dot structures. The targeted results of this investigation concern (i) the identification of various coordination/dative and noncovalent interactions in the halide perovskites and their subsequent characterizations, (ii) the estimations of the natures and strengths of such interactions and their importances in the rationale designs, (iii) the prediction and elucidation of the structural accuracies and energetic stabilities of the perovskite species in aqueous environments, and their relation with the corresponding gas phase properties, and, (iv) the exploration of whether or not the chemical physics of the small model clusters examined can adequately assist in understanding the large scale 2D/3D images of the halide perovskites.

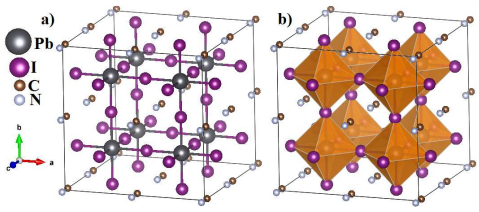

Fig. 1: The a) ball and stick, and b) polyhedral models of the pseudocubic phase of the $MAPbI_3$ perovskite, analogous with the one reported in the solid state (Cambridge Structural Database (CSD) ref. code MAPBTI02). Both displays the facial part of each PbI_6^{4-} octahedron is equipped with an MA cation. For clarity, the H atoms are not shown.

[**Results and Discussions**] In the MAPb(/Sn/Ge)X_3 (X = Cl, Br, I) perovskites in higher dimensions, regardless of their structural diversities (monoclinic, orthorhombic, tetragonal, or pseudocubic), the eight faces of the $[PbX_6]^{4-}$ corner sharing octahedron are perhaps equipped with eight organic cations. For clarity, the attribute is displayed in Fig. 1 for the pseudocubic phase of the $MAPbI_3$ perovskite (also see Fig. 1 of abstract *3E04* for monoclinic phase). In any circumstances, the organic cations play a role similar to that of spacers, or soft-glues, or clamps, which assist in holding the $[PbX_6]^{4-}$ octahedra together in layers in the 2D/3D perovskite films. In its simplest representation, no matter whether solid/gas, the geometrical structure of any MAPb(/Sn/Ge)X_3 perovskite is a combination of two species, the $[Pb(/Sn/Ge)X_3]^-$ inorganic core (a strong base), and the $CH_3NH_3^+$ organic surrounding (a strong acid). This can be realized from Fig. 2, illustrated for the $CH_3NH_3PbI_3$ cluster, for example. Clearly, the unified arrangement is the result of the marriage between an acid and a base comprising polarities of two kinds. This is of course driven by the donation of an appreciable

amount of electron densities (~ 0.2–0.3 *e*) from the electron rich orbital of the anion to an empty orbital of the cation. A consequence of this is an emergence of an extensive network of hydrogen bonding interactions operated by electrostatics forces. Evidently, whatever the occasion is, the absence of the above-mentioned attractive interactions would not allow the halide perovskites to have any real physical existence.

While it is not possible here to discuss the detailed structural and energetic stability preferences between all kinds of the halide perovskites examined, we present only the results of the $CH_3NH_3PbI_3$ clusters. The M06-2X/ADZP and PBE/ADZP binding energies for the most stable $CH_3NH_3PbI_3$ cluster were computed to be –125.1 and –129.2 kcal mol^{-1}, respectively. The slight variation in the binding energy is not unexpected as the percentages of exchange and correlation mixing in the two DFT functionals are different. The binding energy can be tunable depending on the physical orientation of the MA species around the facial part of the PbI_3^-. Accordingly, such an orientation has led to the formation another three conformers whose energies nonetheless are not small, values lying between –95.1 and –129.2 kcal mol^{-1} with PBE/ADZP, and that between –93.5 and –125.1 kcal mol^{-1} with M06-2X/ADZP (see Fig. 2 for conformational details). Indeed these energies are orders of magnitude larger than the range of values known for noncovalent interactions, varying in strength from very weak (–0.2 and –0.5 kcal mol^{-1}) to extremely strong (e.g., –40.5 kcal mol^{-1} for F^-•••H–F). The result enables us to conclude that the I•••H–N and I•••H–C hydrogen bonding interactions emanated of the halide perovskites are *not just ordinary ionic interactions*, but are rare, specific, directional and contain significant amount of covalent character. Of course, electrostatics, induction, polarization, and dispersion interactions, etc., together with solvation, crystal packing forces, among others, are the key cornerstones collectively providing rigidity to the entire geometries of the perovskite films in the crystalline phase.

Fig. 3 illustrates the energy-minimized geometries of the $[PbX_6]^{4-}$ bare ion, and its multinary clusters with MA. Despite several attempts, the cluster of PbI_6^{4-} with a single MA species, as well as that with three MA species, could not be energy-minimized. While the first arrangement led to the dissociation of the PbI_6^{4-} octahedron (upon its interaction with the MA species), the latter arrangement involving the three MA species resulted in frequent convergence error. A similar failure was also noticed when the two MA subunits were asymmetrically placed around the PbI_6^{4-} core. However, with some effort the geometry optimization of the latter arrangement resulted in a clustered species comprising the tetrahedral PbI_4^{2-} and the I^-•••$^+CH_3NH_3$ hydrogen bonded ion-pairs, Fig. 3b). The abnormal feature was not turned on when two MA species were placed symmetrically around the two faces of the PbI_6^{4-} core, with the computed binding energy of –558.8 kcal mol^{-1} for the resulting cluster, see Fig. 3c). This result is analogous to an experimental observation of Leguy et al. who have found that the hydration process is isotropic and homogeneous throughout the perovskite film.[7a)] Nevertheless, as might be realized from Fig. 3, the (stepwise) binding energy monotonically increases from –558.8 to –941.3 kcal mol^{-1} by increasing up to six MA species around the PbI_6^{4-} ion. Adding more MA species (i.e., increasing the number of MA species from 6 through 7 to 8) around the PbI_6^{4-} ion has resulted in a decreasing tendency for the binding energy, with ΔE becoming –785.8 kcal mol^{-1} for the $[PbI_6(CH_3NH_3)_8]^{4+}$ cluster (for full energetic details see Fig. 3), a consequence of steric crowding. Full structural, and charge transfer features for all the clusters will be discussed in detail during the course of the presentation.

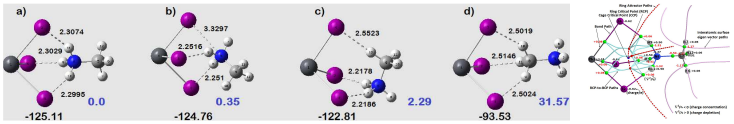

Fig. 2 The M06-2X/ADZP conformations of the $CH_3NH_3PbI_3$ binary cluster, a)–d). Shown are the relative energies (numbers in blue in kcal mol^{-1}), the binding energies (numbers in bold black in ΔE/kcal mol^{-1}), and some selected intermolecular bond distances (numbers in bold black in Å) for the clusters. The graphic on the extreme right represents the QTAIM molecular graph for the most stable conformer a), obtained with the same level of theory. Among some properties, it illustrates the (3,-1) bond (ring and cage) critical points, the bond paths in atom colors connecting bonded atomic basin paths, and the basin gradient paths.

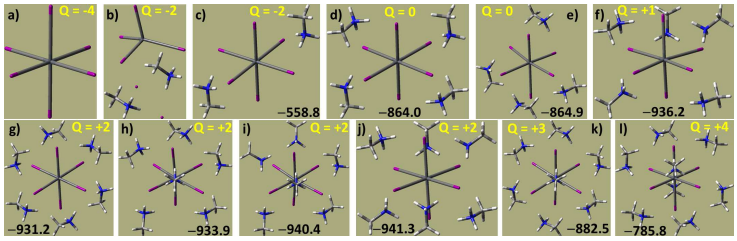

Fig. 3: PBE/DZP energy minimized geometries of the clusters of PbI_6^{4-} with MA. These include a) $[PbX_6]^{4-}$ (*O*$_h$), b) $(CH_3NH_3)_2^{2+}$•2I^-•$[PbX_4]^{2-}$ (*C*$_i$), c) $(CH_3NH_3)_2^{2+}$•$[PbX_6]^{4-}$ (*C*$_i$), d–e) $(CH_3NH_3)_4^{4+}$•$[PbX_6]^{4-}$ (*C*$_i$, *C*$_i$), f) $(CH_3NH_3)_5^{5+}$•$[PbX_6]^{4-}$ (*C*$_i$), g–j) $(CH_3NH_3)_6^{6+}$•$[PbX_6]^{4-}$ (*S*$_6$, *C*$_i$, *C*$_s$, *C*$_i$), k) $(CH_3NH_3)_7^{7+}$•$[PbX_6]^{4-}$ (*C*$_i$), and l) $(CH_3NH_3)_8^{8+}$•$[PbX_6]^{4-}$ (*C*$_i$), where the terms in *italics* represent the point group symmetries. Shown are the net charges (Q/e) and the overall binding energies (kcal mol^{-1}) of latter ten cluster systems.

The HOMO-LUMO gaps in molecules, as well as in molecular clusters, represent the difference in energies between the highest occupied and the lowest unoccupied molecular orbitals. It has comparable significance with band gap generally referred in the solid state. For the latter, the gap represents the energy difference between the top of the valence band and the bottom of the conduction band. Benchmark calculations comprising 35 DFT functionals, together with the HF and MP2 methods, were performed to assess their dependences on the HOMO-LUMO gaps for the most and least stable $CH_3NH_3PbI_3$ clusters (see Fig. 1). Majority of the functionals incorporating 0–22 % Hatree-Fock exchange have predicted the energy gap in the 2.07 – 4.24 eV range for the clusters, comparable with the PBE/DZP estimates; all utilized the M06-2X/ADZP optimized geometries for the two clusters. The gap is a little affected for the $[(CH_3NH_3)_{n=0,2,4\text{-}8}PbI_6]^{Q=-4\text{ to }+4}$ and $[(CH_3NH_3)_8PbI_6]^{4+}$•$(H_2O)_{n=1-10}$ octahedral clusters, all < 3.3 eV with PBE/DZP. The large optical gap for the (0D) quantum dot perovskite materials is not very astonishing as such gaps have strong dependence on the dimensionality, that is, it increases with the size of the perovskite material passing from 3D to 2D to 1D to 0D. All the results above suggest that the gas phase calculations do provide an additional dimension that enhances the current understanding of the novel physical chemistry of the organic-inorganic halide perovskite solar cell materials, probably consistent with others.[7b)–c)]

[References]

[1] S. D. Stranks et al., Nat. Nanotech. 2015, 10, 391.

[2] The future of low-cost solar cells. M. Jacoby, C & EN news, 2016, 94, 30.

[3] a) M. M. Lee, Science 2012, 338, 643; b) T. -B. Song et al., J. Mater. Chem. A 2015, 3, 9032.

[4] a) J. S. Manser et al., Acc. Chem. Res. 2016, 49, 330; b) B. Saparov et al., Chem. Rev. 2016, 116, 4458; c) D. Li et al., J. Phys. Chem. C 2016, 120, 6363; d) J. M. Frost, Nano Lett. 2014, 14, 2584; e) T. A. Berhe et al., Energy Environ. Sci. 2016, 9, 323.

[5] J. Yan, B. R. Sounders, RSC Adv. 2014, 4, 43286; b) T. C. Sum et al., Acc. Chem. Res. 2016, 49, 294.

[6] a) C. C. Stoumpos, M. G. Kanatzidis, Adv. Mat. 2016, 28, 5778; b) For details see the editorial text "focus on perovskite solar cells" available at: http://iopscience.iop.org/journal/0957-4484/page/Focus-Perovskites.

[7] a) A. M. A. Leguy at al., Chem. Matt. 2015, 27, 3397; b) Y. H. Chang, J. Kor. Phys. Soc. 2004, 44, 889; d) Fang et al., J. Phys. Chem. Lett 2016, 7, 1596; c) G. Giorgi, K. Yamashita, J. Phys. Chem. Lett., 2016, 7, 888.

3E04

On the environmental stability of methylammonium lead/tin halide ($CH_3NH_3Pb(/Sn)X_3$) perovskites

(Department of Chemical System Engineering, School of Engineering, The University of Tokyo, 7-3-1 Hongo, Bunkyo-ku, Japan 113-8656)

[O] Arpita Varadwaj, Pradeep R. Varadwaj, Koichi Yamashita

E-mail: arpita@tcl.t.u-tokyo.ac.jp

[Introduction] Scientists categorize methylammonium lead(/tin) trihalides as possible potential candidates for the third-generation of photovoltaic solar cells.[1] They are represented by the chemical formula $CH_3NH_3Pb(/Sn)X_3$ (X = Cl, Br, I). They are soft nanomaterials, which are a class of hybrid minerals formed of an unusual mixing of two different ionic species, the $CH_3NH_3^+$ organic cation and the $[Pb(/Sn/Ge)X_3]^-$ inorganic anion, which are the key ingredients for the building block. The above formula belongs to the ABX_3 perovskite family; the most common one in this family is discovered to be $CaTiO_3$. Clearly, the formulations above possess structural similarities that explain why the mixtures comprising the lead or tin trihalides and the methylammonium are referred to as organic-inorganic hybrid perovskites. Notable is their extraordinary mechanical and technological breakthroughs for which they have gone viral in academics, as well as in the solar sector today.[2] For instance, the halide perovskites display large optical (photo) absorption coefficients > 16 mm^{-1}.[2] They carry giant static dielectric constants ranging between 60 and 70, low exciton binding energies approximately close to 16 meV at low temperatures, exceptional minority carrier lifetimes close to 280 ns, long electron and hole diffusion lengths up to 175 microns, high charge carrier mobilities < ~100 $cm^2/(Vs)$, and very low effective masses of electrons and holes (viz. tetragonal: 0.197 vs. 0.340 m_0; orthorhombic: 0.239 vs. 0.357 m_0), excellent for transport.[3]

An attribute exposing the halide perovskites to scientific communities is photovoltaic conversion efficiency (PCE). (The term *efficiency* refers a fraction of sunlight energy converted to the electrical energy *via* the photovoltaic technology.) The National Renewable Energy Laboratory (NREL) certified PCE ranges up to 22.1%, reported early this year.[4] This is indeed a fantastic improvement compared not only to the prior value of 3.8% reported for the first time in 2009,[5] but also to the crystalline silicon solar cells that have taken decades to reach a PCE somewhat closer to the above value. It is recently showed that when the mixed cesium cation lead mixed-halide perovskite tendem solar cells combine with the 19%-efficient silicon solar cell, it would result in the feasibility of achieving an efficiency of conversion even greater than 25%.[5] Nevertheless, an obvious feature that lifts the perovskite materials to a top level lies in a measurable property called optical band gap energy. It is tunable in the 1.5 to 3.1 eV range, with a value of < 1.6 eV being recommended for device performance. The featured characteristics mentioned above, together with their excellent transport properties, might explain why the halide perovskites do have propitious potentials to serve as p–i–n type semiconductor junction (photo)diodes. Nonetheless, many researches are currently ongoing in this filed to identify factors influencing the chemico-technological improvement of the PCE, the origins of anomalous hysteresis in the current–voltage characteristics, and the origins of the ferroelectricity, etc., observed for the highest efficient lead iodide perovskite. In contrary, several other researchers are involved to explore factors responsible explaining the observed air and moisture instabilities of the $CH_3NH_3Pb(/Sn)X_3$ perovskite films. Whilst a number of experimental observations on the latter topic have led to diverse views, there is almost no theoretical attempt placed to insight into the chemical physics of the anhydrate perovskites in water (H_2O). Herein, we report the electronic structure, binding energy, molecular band gap, and electron density topological property results of several hydrated clusters of the $[Pb/SnI_6(MA)_8]^{4+}$ cation in zero-dimension, where MA refers to $CH_3NH_3^+$. These results are achieved combining Density Functional Theory (DFT) with Quantum Theory of Atoms in Molecules (QTAIM) calculations. Finally, the results are compared with those already reported for the $MAPb(/Sn)X_3$ perovskites in higher dimensions. The study has boosted us concluding whether or not the environmental species, e.g. H_2O, is fully responsible for degrading the halide perovskites.

[Results and discussions] Two conflicting views are advised in the literature in connection with the environmental stabilities of the halide perovskites. According to a bunch of authors, including Mitzi and colleagues,[6b] Kamat and coworkers,[6a] and others,[6c)–e)] the halide perovskites are not air, moisture, and humidity stable because they are highly sensitive to the environment. According to Frost et al., [6d] a single water molecule is sufficient to degrade the halide perovskites when it comes into contact with, but an excess of it would dissolve the HI and CH_3NH_2 byproducts, as well as to degrade the material completely to form PbI_2. Perhaps this suggestion is consistent with those of Kamat et al. and others.[6a] For instance, these latter authors have suggested that the possible reaction pathway for the decomposition of the $CH_3NH_3PbI_3$ perovskite in the presence of H_2O is: $CH_3NH_3PbI_3$ (solid) ⟶ CH_3NH_2 (gas) + HI (gas) + PbI_2 (solid). The $CH_3NH_3PbI_3$ species upon its exposure to moisture forms mono- and di-hydrates, $CH_3NH_3PbI_3{\bullet}H_2O$ and $(CH_3NH_3)_4PbI_6{\bullet}H_2O$, respectively, as the integral parts of the degradation mechanism. And that the introduction of the H_2O molecule into the geometry of the lead iodide perovskite not only result in the widening of the band gap of the material, but also changes its surface morphology.

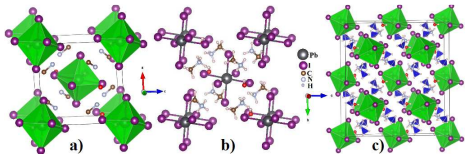

Fig.1. The a) polyhedral, and b) ball and stick models for the packing of the $(CH_3NH_3)_4PbI_6{\bullet}2H_2O$ crystal as of the Cambridge Structure Database (CSD) (ref. code FOLLIB). Shown in c) is a 1x2x3 slab model of the aforesaid crystal reported by Wakamiya et al. (CSD ref. code, FOLLIB01). For clarity, H atoms are omitted in a).

Oppositely, a recent experimental investigation of Manshor et al. demands that the $CH_3NH_3PbI_3$ film is only *a little* affected upon its exposure to humidity.[7a] Its major degradation occurs when it is exposed with photon dose. This conclusion was drawn after the $MAPbI_3$ pristine films were exposed separately to both dark and light. It made the film to result in more intense degradation despite their ~7 times shorter shelf-life (~ 100 h) in light relative to that observed in the dark (~ 600 h). Contrariwise, when the authors exposed the $CH_3NH_3PbI_3$ PeP films to humidity in dark, they did not observe the presence of the PbI_2, suggesting the film was not degraded. However, the authors did observe a change in the color of the film from dark to light brown, which they recognized as a consequence of structural variations in the film. Note that when the 5, 10, and 20 wt% films of the latter type were placed in light, they underwent significant degradation especially in the interface region formed between the TiO_2 electron transport layer and the perovskite films, consistent with observations of others.[7b)–c)] These were contradictory with those the pristine films exposed to similar environments, which resulted in complete degradation of the films leading to PbI_2. Consequently, these results propagandize the degradation of both the film types mainly by photon dose under humid condition.

Nevertheless, there are about three crystallographic structures reported for hydrated $CH_3NH_3PbI_3$, catalogued in the Cambridge Structural Database (CSD). These include one $CH_3NH_3PbI_3{\bullet}H_2O$[8a] and two $(CH_3NH_3)_4PbI_6{\bullet}2H_2O$.[8b)–c)] The former and latter structures reported in 1987 and 2014 are having P21/n and P21/m space group symmetries, respectively. Figs. 1 a) & c) display the packed polyhedral, and b) the ball & stick models of the $(CH_3NH_3)_4PbI_6{\bullet}2H_2O$ crystal reported in 1987,[8b] consisting of a distorted fcc array of the PbI_6^{4-} ions interspersed with the $CH_3NH_3^+$ cations of two types and H_2O molecules of a single type. Fig. 1 c) shows a 1x2x3 slab model for the hydrated structure reported by Wakamiya and coworkers, [8c] displaying the structural evolution of the unit cell, which has identical stoichiometry relative to the crystal reported in 1987,[8b] and that the H_2O molecules in this crystal were introduced by exposing the sample to air. Nevertheless, as displayed in Fig. 1, both the crystals contain several PbI_6^{4-} octahedra in higher dimension in which the each of the eight faces of a given octahedron can be realized

equipped with an MA species, that is, $[PbI_6(MA)_8]^{4+}$. The attribute is not only reminiscent of the crystal of $CH_3NH_3PbI_3$ in the monoclinic phase, but also evident of its other known phases (viz. see *abstract 3E03* for the pseudocubic phase).

While many possibilities exist, five conformers for each of the $[Pb(/Sn)X_6(MA)_8]^{4+}$ cations were optimized with DFT-PBE/DZP, see Fig. 3a). The most stable of these in each set is found to be a structure with center of inversion symmetry, C_i, $[Pb(/Sn)I_6(MA)_8]^{4+}$. The physical orientations of the $CH_3NH_3^+$ cations around the first coordination sphere of the $[PbX_6]^{4-}$ anion in this stable cluster are similar to that of the $(CH_3NH_3)_4^{4+}\bullet[PbI_6]^{4-}\bullet(H_2O)_2$ crystal, CSD ref. code FOLLIB. Its geometry is about 5.5, 24.7, 24.8, and 103.8 kcal mol^{-1} relatively more stable than the four other high energy conformers identified (Fig. 3a)). Of these latter four, the geometries of the intermediate two are first and second order saddle points, and the other two are genuine local minima. In all the high energy clusters, the eight organic cations facing the centers of the eight faces of the $[PbX_6]^{4-}$ octahedron are perhaps significantly hydrogen bonded.

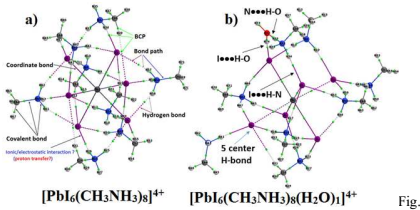

Fig. 2: Examples of QTAIM molecular graphs of the anhydrate (a) and hydrated (with one H_2O molecule) clusters of the $[PbI_6(CH_3NH_3)_8]^{4+}$ cation, unraveling weak-to-strong interactions.

As already noted, the main focus of this investigation was to theoretically assess how, and to what extent, the $[PbI_6(MA)_8]^{4+}$ coordination sphere can be affected by adding ten H_2O molecules around its surrounding, one at a time systematically in a stepwise manner. Since the DFT-PBE/DZP method (relative to many other DFT functionals and basis sets) produces the molecular HOMO-LUMO gap energy for the zero-dimensional $CH_3NH_3PbI_3$ cluster somehow closer to experimental band gaps reported for the higher dimensional analogues, the same method was utilized for the energy-minimization of the $[Pb(/Sn)X_6(MA)_8]^{4+}$ (X = Cl, Br, I) octahedra. Later, the H_2O molecules were added one by one to the outer second coordination spheres of each of the $[Pb(/Sn)X_6(MA)_8]^{4+}$ systems in a stepwise manner. The process was continued until all the $[(Pb(/Sn)I_6(MA)_8)\bullet\bullet\bullet(H_2O)_{n=1-10}]^{4+}$ cationic clusters were fully energy minimized.

While the knowledge of the positions of the H atoms in MA in the $(CH_3NH_3)_4PbI_6\bullet 2H_2O$ crystal is completely lacking, the nature of hydrogen bonding interactions discussed in the literature is purely arbitrary.[8b)] Fig. 2 depicts QTAIM molecular graphs for two selected clusters, the anhydrate $[PbI_6(MA)_8]^{4+}$ and the (single water) hydrated $[PbI_6(MA)_8(H_2O)_1]^{4+}$. It has greatly assisted us in identifying various kinds of such interactions, consistent with the recommended IUPAC signatures. For instance, the anhydrate cluster is stabilized by means of an extensive network of I•••H─N(MA) and I•••H─C(MA) intermolecular hydrogen bonded interactions, in which each MA involves in three of them. Such identifications are relied on the presence of the bond critical points (BCPs) of charge density between atomic basins, and the bond paths that connect them, and the short-to-long intermolecular distances for the above interactions (2.427─2.660 vs. 2.832–3.530 Å). The short I•••H─N distances explain the $–NH_3$ part of MA is prone to reaction as is always observed tilted towards the face center, or the corner, or the edge of the octahedron in majorities of the halide perovskites crystals catalogued.

Upon an addition of a single H_2O molecule to the second coordination sphere of the $[PbI_6(MA)_8]^{4+}$ ion, the geometry of the ion in the modified species is distorted, but it is not very significant that can degrade the close-shell system completely, as suggested.[6d)] As in Fig. 2b, a single H_2O molecule upon its introduction has displayed its sufficient potential to leak into the second coordination shell formed of the MA ions. A consequence of this is that the highly competitive hydrogen bonding interactions between I and H_2O, MA and H_2O, and I and MA experience significant push-ups due to steric reasons, leading the MA ions (compared to the H_2O) to move further away. The result explains why some of the MAs in Fig. 2 govern singular hydrogen bonding interactions with the I atoms in $[(CH_3NH_3)_8^{8+}\bullet[PbI_6]^{4-}\bullet(H_2O)_1]$.

The I atoms in $[PbI_6]^{4-}$ serve as four- and/or five-center hydrogen bond acceptors in presence of H_2O, an unified feature that has never enlightened before. Since the H_2O species is smaller than MA and has an adamant of forming hydrogen bonding interactions, it forms two such interactions with its two proton donors upon its interaction with the I atoms in $[(CH_3NH_3)_8[PbI_6]^{4+}$. In the meantime, as an acceptor of hydrogen bonds, the O atom of it simultaneously involves in predominant proton transfer reactions with the protons of the $–NH_3$ fragment in MA. Because of this latter feature, and because of the presence of unavoidable steric crowding between the H_2O and MA species in the second coordination sphere, the latter species will be pushed backward. This situation is displayed in Fig. 2 (right). Note that the addition of more H_2O molecules to the second coordination sphere of the $[(PbI_6(MA)_8)]^{4+}$ ion results in the facilitation of significant proton transfer reactions between the H_2O molecules and the MA species in the modified clusters. At this stage, if the perovskite material is exposed with significant photon dose, or with high temperatures, it would probably undergo significant structural decomposition. Through this way, there are significant chances for the sublimation of various species, e.g., NH_3CH_3I, CH_3NH_2 and HI, etc., leaving the PbI_2 solid species alone.

A single H_2O molecule on the outer sphere of the $[(PbI_6(MA)_8)]^{4+}$ cation produces an uncorrected binding energy ΔE of –40.2 kcal mol^{-1}. Successive increase in the number of H_2O molecules around the cation increases the ΔE values for the hydrated cluster ions. The trend in increase in ΔE is non-additive cooperative. The most stable cation has ten H_2O molecules, $[(PbI_6(MA)_8)\bullet\bullet\bullet(H_2O)_{10}]^{4+}$, with $\Delta E \sim –291.0$ kcal mol^{-1} (roughly –29.1 kcal mol^{-1} per H_2O). Fig. 3 shows a linear relationship between the number of the H_2O molecules n in the $[(Pb(/Sn)X_6(MA)_8)\bullet\bullet\bullet(H_2O)_{n=1-10}]^{4+}$ ion and the ΔE. The graphs indicate that although the H_2O molecules distort the geometries of the $[(Pb(/Sn)X_6(MA)_8)]^{4+}$ ions, they increase the overall stabilities of the hydrated clusters at 0 or 298.15 K. At this range of temperatures, the perovskites might not degrade completely. The conclusion is also decisive regardless of the dimensionality of the halide perovskites.

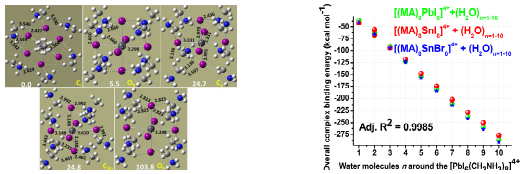

Fig. 3 a) The conformers of the $[PbI_6(MA)_8]^{4+}$ ion & b) the linear dependence of overall binding energy on the number of H_2O molecules n for the $[[PbI_6(CH_3NH_3)_8]\bullet\bullet\bullet(H_2O)_{n=1-10}]^{4+}$ clusters. The data points are fitted to a linear equation of the form: $\Delta E = a\times n + b$.

The HOMO-LUMO gap is an important measure of the device quality of a material. Its value for $[(PbI_6(MA)_8)]^{4+}$ is PBE/DZP calculated to be 3.07 eV. Addition of two H_2O molecules (first and second) around the coordination sphere of the ion has downshifted the gap to 2.65, and 2.62 eV, respectively. However, increasing this number to three (or, even up to ten) around the $[(PbI_6(MA)_8)]^{4+}$ ion, the gap further increases in which the gap oscillates between 3.05 and 3.25 eV for all the cationic clusters investigated. For instance, the value of this gap was ca. 3.09, 3.13, 3.25 and 3.24 eV for $[(PbI_6(MA)_8)\bullet\bullet\bullet(H_2O)_3]^{4+}$, $[(PbI_6(MA)_8)\bullet\bullet\bullet(H_2O)_4]^{4+}$, $[(PbI_6(MA)_8)\bullet\bullet\bullet(H_2O)_6]^{4+}$ and $[(PbI_6(MA)_8)\bullet\bullet\bullet(H_2O)_{10}]^{4+}$, respectively. This may mean the optical gap is almost unaffected by the presence of the H_2O molecules despite the significant geometrical distortions encountered. The conclusions drawn above for the $[PbI_6(MA)_8]^{4+}$ hydrated systems can be applicable to the other hydrated clusters, viz. $[PbX_6(MA)_8]^{4+}$ (X = Cl, Br) and $[SnX_6(MA)_8]^{4+}$ (X = Cl, Br, I).

[References]

[1] a) J. Yan, B. R. Sounders, RSC Adv. 2014, 4, 43286; b) T. C. Sum et al., Acc. Chem. Res. 2016, 49, 294.

[2] T. -B. Song et al., J. Mater. Chem. A 2015, 3, 9032.

[3] a) Miyata et al, Nat. Phys. 2015, 11, 582; b) R. E. Brandt, V. Stevanović, D. S. Ginley, T. Buonassisi, MRS Commun. 2015, 5, 265; c) T. M. Brenner, D. A. Egger, A. M. Rappe, L. Kronik, G. Hodes, D. Cahen, J. Phys. Chem. Lett. 2015, 6, 4754.

[4] See the photovoltaic solar cell chart at: http://www.nrel.gov/ncpv/images/efficiency_chart.jpg

[5] a) McMeenkin et al., Science 2016, 351, 151; b) S. Yakunin et al., Nat. Photonics 2015, 9, 444.

[6] a) J. S. Manser et al., Acc. Chem. Res. 2016, 49, 330; b) B. Saparov et al., Chem. Rev. 2016, 116, 4458; c) D. Li et al., J. Phys. Chem. C 2016, 120, 6363; d) J. M. Frost, Nano Lett. 2014, 14, 2584; e) T. A. Berhe et al., Energy Envirno. Sci. 2016, 9, 323.

[7] a) N. A. Manshor et al., Phys. Chem. Chem. Phys.2016, DOI: 10.1039/C6CP03600G; b) F. Matsumoto, J. Phys. Chem. C 2015, 119, 20810; c) J. Xiong et al., Org. Electron. 2016, 30, 30.

[8] a) F. Hao et al., J. Am. Chem. Soc. 2014, 136, 16411; b) B. R. Vincent et al., Can J. Chem. 1987, 65, 1042; c) A. Wakamiya et. al., Chem. Lett. 2014, 43, 711.

3E05

広視野フェムト秒光散乱顕微分光による有機-無機ペロブスカイト単一微粒子の励起子ダイナミクス

（関学大・理工）○片山哲郎、末永晴信、奥畑智貴、玉井尚登

Exciton dynamics of a single colloidal perovskite nanoparticle by means of widefield femtosecond light scattering microscopy

(Kwansei Gakuin Univ.) ○Katayama Tetsuro, Suenaga Harunobu, Tomoki Okuhata, Tamai Naoto

【序】TiO_2 を電子電導層に用いた色素増感太陽電池のなかで、$(CH_3NH_3)PbX_3$(X=I, Br, Cl)を光吸収層に用いた有機-無機ハイブリッド系は、20%に至るまで飛躍的に光電変換効率が向上し、注目されている系である。この系の高い光電変換効率は、10^5 $M^{-1}cm^{-1}$ 程度の高い分子吸光係数および長い励起子拡散長に起因した高い電荷分離反応効率に起因すると報告されてきた。近年、顕微鏡下の過渡吸収測定により、ペロブスカイト型の電池においてその励起子ダイナミクスがペロブスカイト結晶の形態によって大きく変わることが報告されており[1]、特に、ナノ粒子系ではその結晶サイズ、形態によって、比較的低い閾値でレーザー発振をするなど、特異的な発光性が報告されている[2]。一方で結晶のサイズ、形態毎に大きくその性質が異なるため、個々の粒子を分離し、それぞれの励起子ダイナミクスを研究する必要があるが、実験的な困難さを伴うため、これら結晶形態と励起子ダイナミクスは未だ明らかでない点が多い。そこで、本研究では単一粒子の測定を可能とする全反射型の顕微過渡散乱測定装置を構築し、単一のペロブスカイトナノ粒子系の励起状態ダイナミクスを解析したので報告する。

【実験】$CH_3NH_3PbBr_3$ ナノ粒子の試料合成には再沈法を用いた[3]。CH_3NH_3PbBr(0.16 mmol)、$PbBr_2$(0.2 mmol)、n-octylamine (20 μL)、オレイン酸 0.5 mL を DFM (5 mL)溶媒に加え作製した前駆体の溶液を、マイクロシリンジを用いて 10 mL のトルエン溶媒に加えた。その後、7000 rpm の速度で 10 分間の遠心分離を行い作製した。室温下で作製した量子ドットに対して透過型電顕測定を行った結果、平均粒径は 5.5 nm であった。

$CH_3NH_3PbBr_3$ の微小結晶の作製にはまず、酢酸鉛三水和物水溶液(100 mg/mL)をガラス基板上にたらし、65℃で 30 分乾燥させ結晶化させた。その後、結晶の付着したガラス基板を $CH_3NH_3PbBr_3$ イソプロパノール溶液 1 mL に 20 時間浸し、イソプロパノールで洗浄した。ナノ粒子の観察には透過型電子顕微鏡 (FEI-tecnai 20, 加速電圧 200 kV)を用いた。

フェムト秒顕微過渡散乱測定、フェムト秒過渡吸収スペクトル測定では再生増幅器一体型の Ti:Sapphire レーザー (Solstice, Spectra Physics, 800 nm)を光源として用いた。励起光および観測光は非同軸パラメトリック増幅器(NOPA, TOPAS - White, Light Conversion) を用いて波長変換し、プリズム対を用いて群速度分散の補正を行った。スペクトル測定における観測光は 1000 nm に変換したのち光学遅延台を通し、CaF_2 板に集光し発生させた白色光を用いた。検出器には顕微鏡下の測定では CCD カメラ(Pike-32B, Allied Vision Technologies)、溶液のスペクトル測定にはマルチチャ

ンネル分光器(PMA20, Hamamatsu Photonics) を用いてデータ収集し、機器の制御には Labview (National Instruments) 上の自作プログラムを使用した。

【結果と考察】図 1 に $CH_3NH_3PbBr_3$ 微粒子のフェムト秒顕微過渡散乱測定結果の一例を示す。図 1(a)は観測光 515 nm を照射したときの全反射散乱画像である。図 1(b)は 480 nm の励起フェムト秒パルスを照射し、それぞれ①、②の位置座標に対応した過渡散乱強度の時間変化である。過渡散乱強度は、粒子毎に異なる挙動を示した。①と②の粒子では 2 ps 以降では散乱強度の正負が異なる挙動を示した。このことは粒子毎に異なる励起子ダイナミクスがあることを示している。

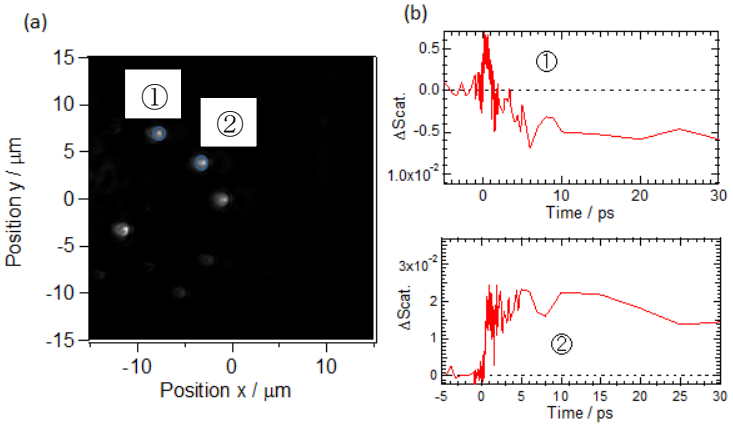

図 1 顕微過渡散乱測定による(a) $CH_3NH_3PbBr_3$ 微粒子の散乱画像および(b)①、②の座標の過渡散乱強度の時間変化(Exc. 480 nm, Mon. 515 nm)

この挙動を理解するために、トルエン溶媒中の $CH_3NH_3PbBr_3$ 微粒子の過渡吸収スペクトル測定を行った。図 2 に室温、および 283 K で作製したトルエン溶媒中の $CH_3NH_3PbBr_3$ 微粒子の励起後 100 ps の過渡吸収スペクトルを示す。室温で作製した(平均粒径 5.5 nm)の $CH_3NH_3PbBr_3$ 微粒子では、515 nm 付近に負の吸収極大を持つスペクトル形状を示した。この負の信号は基底状態の減少量に対応するブリーチ信号に帰属される。一方、283 K で合成した $CH_3NH_3PbBr_3$ 微粒子では、ブリーチ信号の吸収極大波長が 515 nm より短波長側に表れた。室温よりも低温条件下で $CH_3NH_3PbBr_3$ 微粒子を作製した場合、粒子のサイズが小さくなるため吸収および発光スペクトルがブルーシフトすることが報告されており[4]、今回のブリーチ信号の吸収極大波長の変化も粒径サイズが小さくなることに起因すると考えられる。このブリーチ信号のブルーシフトにより 283 K で作製した試料では 515 nm 付近で正の値を示ししている。したがって、顕微過渡散乱測定で観測された粒子毎に正負の異なる信号挙動は、試料の粒径サイズを反映したものであることが示唆される。発表ではこれら量子ドット系の不均一な励起子ダイナミクスに加え、$CH_3NH_3PbBr_3$ ナノワイヤーにおける励起子ダイナミクスについても議論する予定である。

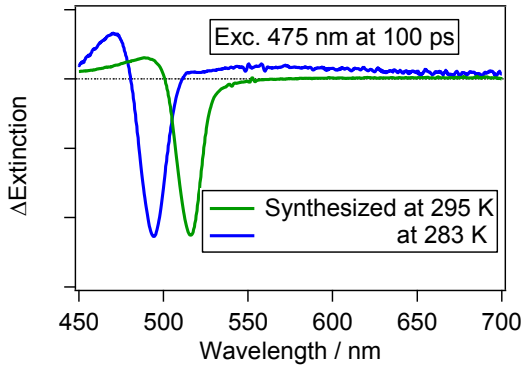

図 2 $CH_3NH_3PbBr_3$ 微粒子トルエン溶液の励起後 100 ps における過渡吸収スペクトル

[1] T. Katayama et al., *Chem. Lett.*, **2014**, *43*, 1656

[2] S. W. Eaton et al., *PNAS,* **2016**, *113*, 1993

[3] F. Zhang et al., *ACS. Nano. Lett.*, **2015**, *9*, 2533

[4] H. Huang et al. *Adv. Sci.,* **2015**, *2*, 1500194

3E06

CdSe-Au ハイブリッドナノ構造体のフェムト秒状態選択励起による電子移動ダイナミクス

（関西学院大院・理工）○奥畑智貴，片山哲郎，玉井尚登

Electron Transfer Dynamics in CdSe-Au Hybrid Nanostructures with Femtosecond State Selective Excitation

(Kwansei Gakuin Univ.)
○Tomoki Okuhata, Tetsuro Katayama, Naoto Tamai

【序】近年、コロイド合成した半導体ナノ粒子(NPs)から外部への電荷抽出に関する研究が盛んに行われてきた。半導体 NPs-アクセプター分子系では、NPs 内における強い電子-正孔相互作用によりマーカスの逆転領域が存在しない高効率電子移動反応が報告されている[1]。また、CdSe ナノプレート(NPLs)-MV^{2+}系では、MV^{2+}が吸着する CdSe NPLs の面の違いによって異なる電子移動速度が観測されることが明らかになった[2]。半導体 NPs に金属 NPs を接合したハイブリッドナノ構造体(HNs)においても効率的な電荷分離が見込まれるため、光エネルギー変換材料への応用に期待されている。しかし、半導体-金属 HNs における電子移動過程の詳細な解析は一部の構造体でしか報告されていない。当研究室では、CdSe ナノロッド(NRs)に Au NPs を接合した系において、CdSe NRs のバンド端状態、および高励起状態から Au NPs への電子移動を解析してきた[3]。また、PbS 量子ドット(QDs)-Au HNs における ps スケールの正孔移動と装置応答関数より速い超高速電子移動を解析した[4]。本研究では、CdSe QDs を用いて CdSe QD-Au HNs を合成し、この構造体における電子移動過程を状態選択励起下でフェムト秒ポンプ-プローブ分光を用いて解析したので報告する。

【実験】オレイルアミンを保護剤として CdSe QDs を合成した。合成した CdSe QDs に Au 前駆体溶液を 0.3 mL 滴下して 10 分間反応させたものを CdSe QD-Au HNs A、0.5 mL 滴下して 20 分間反応させたものを CdSe QD-Au HNs B とした。透過型電子顕微鏡(TEM)を用いて構造解析を行った。Ti:Sapphire レーザーの第二高調波を励起光として用い、フェムト秒過渡吸収測定を行った。状態選択励起は Ti:Sapphire レーザーの基本波を光パラメトリック増幅器(OPA)に導入し、任意の波長に変換したものを励起光として用いた。

【結果と考察】3 次元量子閉じ込め系である CdSe QDs に Au NPs を接合した CdSe QD-Au HNs の TEM 像、および各サンプルの吸収スペクトルを図 1 に示す。CdSe QD-Au HNs B の TEM 像から、粒径(2.0 ± 0.4) nm の Au NPs が CdSe QDs に接合していた。また、CdSe

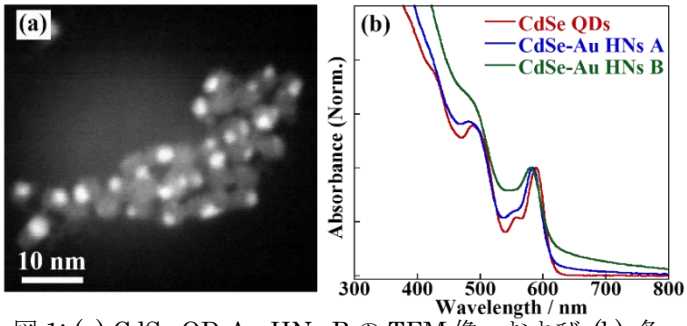

図 1: (a) CdSe QD-Au HNs B の TEM 像、および (b) 各サンプルの吸収スペクトル

QD-Au HNs A においては、Au NPs の粒径は(1.2 ± 0.4) nm であった。CdSe QDs の吸収スペクトルには 589 nm にバンド端(1S)吸収が観測されるとともに、2S 吸収(555 nm)と 1P 吸収(495 nm)も明確に観測された。CdSe QD-Au HNs では、Au NPs の粒径が大きいほうが 1S 吸収がわずかに短波長シフトするとともに、吸収ピークのブロードニングが観測された。また、CdSe QD-Au HNs では CdSe QDs 由来のバンド端発光の顕著な消光が観測された。CdSe QDs のエネルギー準位と Au のフェルミ準位の関係より、CdSe QDs から Au NPs への電荷移動が起こっていると考えられる。

励起波長 400 nm における CdSe QDs と CdSe QD-Au HNs の過渡吸収スペクトルを図 2 に示す。各サンプルの過渡吸収スペクトルには 1S 吸収に対応する波長にブリーチピークが観測され、CdSe QD-Au HNs では CdSe QDs より早くブリーチが回復していた。これは CdSe QDs から Au NPs への電子移動に起因すると考えられる。次に、各サンプルの 1S ブリーチピークにおける過渡吸収ダイナミクス、および 1S ブリーチ収率を図 3 に示す。CdSe QD-Au HNs の 1S ブリーチダイナミクスには、電子移動に対応すると考えられる 1 ps 以内の速い緩和成分が観測された。また、CdSe QDs では 1S ブリーチのライズ成分が 290 fs であったのに対し、CdSe QD-Au HNs では 150 fs 程度のライズが観測されるとともに、CdSe QD-Au HNs の 1S ブリーチの収率が低下していた(図 3(b))。これらの結果は、CdSe QDs の高励起状態から Au NPs へのホット電子移動が起こっていることを示唆している。

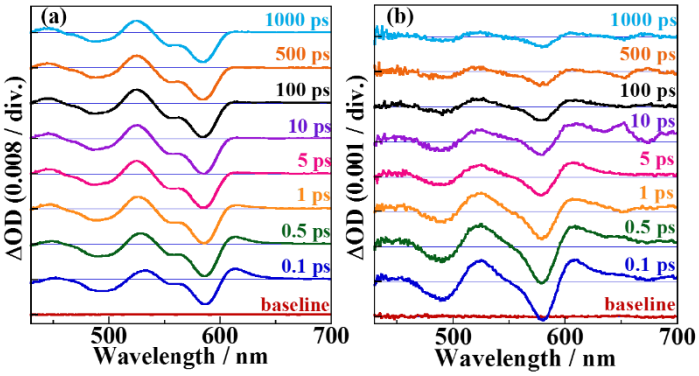

図 2: (a) CdSe QDs、および (b) CdSe QD-Au HNs B の過渡吸収スペクトル (λ_{Ex}: 400 nm)

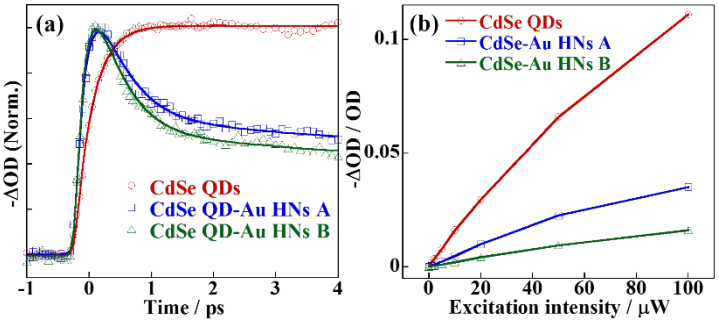

図 3: 励起波長 400 nm での (a) 各サンプルの 1S ブリーチにおける過渡吸収ダイナミクス、および (b) 1S ブリーチの収率

OPA を用いて 1S 状態を選択励起した場合、1S ブリーチは装置応答関数程度で立ち上がっており、この実験条件においてホット電子が生成していないことが確認された。しかし、CdSe QD-Au HNs の 1S ブリーチの収率は、ホット電子移動が起こらないにもかかわらず、CdSe QDs に比べて低下していた。これは、CdSe QDs のバンド端状態において、装置応答関数(~ 60 fs)よりも十分に早い時定数を持つ超高速電子移動が起こっていることを示唆している。2S 状態、および 1P 状態を選択励起した結果についても解析を行い、ホット電子移動の励起波長依存性を詳細に議論する予定である。

[1] Zhu et al., *Nano Lett.* **2014**, *14*, 1263.

[2] Okuhata et al., *J. Phys. Chem. C*, **2016**, ASAP

[3] Sagarzazu et al., *Phys. Chem. Chem. Phys.* **2013**, *15*, 2141

[4] Okuhata et al., *J. Phys. Chem. C*, **2015**, *119*, 2113.

3E07

配位ミネラリゼーション：金属硫化物ヘリックスの合成

（北大院理）○平井健二, 佐田和己

Coordination mineralization: Fabrication of metal sulfide nanohelix

(Hokkaido Univ. Dept. Sci.) Kenji Hirai, Kazuki Sada

【序】

負屈折率材料、偏光板、キラル分子センサーの開発に向けて、キラル発光・吸光特性を有する材料の開発に注目が集まっている。特に、バンド構造由来の幅広い吸収帯を有する無機固体材料は、キラル光学材料として有望な材料群である。無機固体材料を用いてキラル構造を構築する方法としては、キラル有機テンプレートを用いた鋳型合成法が発展してきた。しかしながら、鋳型合成法の報告は、キラルシリカ[1]、キラル酸化チタン[2]などのゾルゲル法による無機酸化物が大多数を占めており、キラル材料の化合物群は限定的である。

金属硫化物は可視光～赤外光に幅広い吸収を有する化合物が数多く報告されており[3]、キラル光学材料に適した化合物が多い。本研究では、ナノスケールで螺旋を巻いた金属錯体を前駆体とすることで、半導体ナノヘリックスの合成法を検討した（**Figure 1**）。具体的には、ペプチドと金属イオンから構成される錯体ナノヘリックスを部分的に加熱分解することによって、金属硫化物/炭素のナノヘリックスへと変換した。また、得られたナノヘリックスの偏光特性の評価を行い、有限要素法によって光学特性を解析することで、ナノ構造体由来の偏光特性の要因を明らかにした。

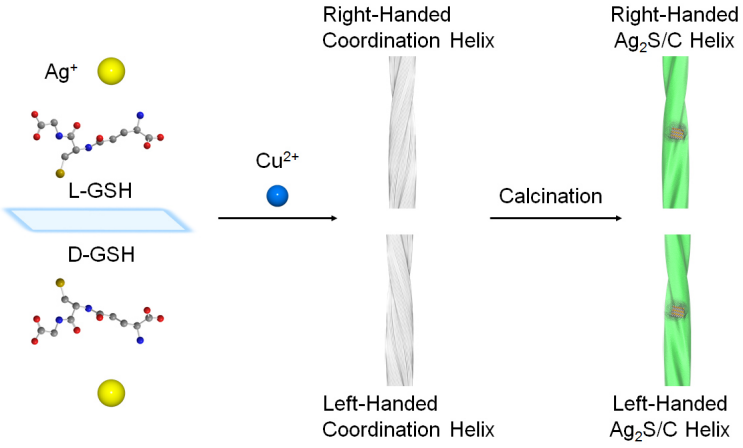

Figure 1. 錯体ヘリックスを前駆体とした金属硫化物/炭素のナノヘリックスの合成

【実験結果と考察】

L-glutathione と過塩素酸銀の水溶液を作製し、混合した後、５日間静置することで錯体ナノファイバーが得られた。この錯体ナノファイバーを硝酸銅溶液中で、１日間撹拌すると、ナノファイバーは螺旋状に集合し、錯体ナノヘリックスが得られた（**Figure 2a**）。L-glutathione から得られた錯体ナノヘリックスは右巻き構造を形成するが、光学異性体である D-glutathione を用いて同様の合成法を行うと、左巻きの錯体ナノヘリックスが得られた。

続いて、得られた錯体ナノヘリックスを窒素下で焼成した。この焼成過程によって glutathione は部分的に分解されるが、錯体ナノヘリックスの形状は維持された。X 線回折測定（XRD）、エネルギー分散型 X 線分析（EDX）により、焼成後に得られたナノヘリックスは $Cu_xAg_{2-x}S$ とアモルファス炭素の複合体であることが明らかとなった。この $Cu_xAg_{2-x}S$/C ナノヘリックスは、L-glutathione を用いることで右巻きヘリックス（R-Cu-Ag_2S/C）を、D-glutathione を用いることで左巻きヘリックス（L-Cu-Ag_2S/C）を選択的に合成することが可能である（**Figure 2b**）。

円偏光二色性(CD)スペクトル測定により、R-Cu-Ag_2S/C と L-Cu-Ag_2S/C は可視光域全体（400-900 nm）にわたって光学活性を有することが明らかとなった。有限要素解析法を用いたシミュレーションにより、短波長側の円偏光二色性は電子遷移に起因しており、長波長側の円偏光二色性は主に光散乱に起因することが示唆された。長波長側の光散乱は Cu-Ag_2S とアモルファス炭素が有する長波長帯での誘電率に大きく依存する。以上の結果より、金属硫化物/炭素のキラルナノ構造体を構築することで、可視光域全体でキラル光学特性を発現することが明らかとなった。

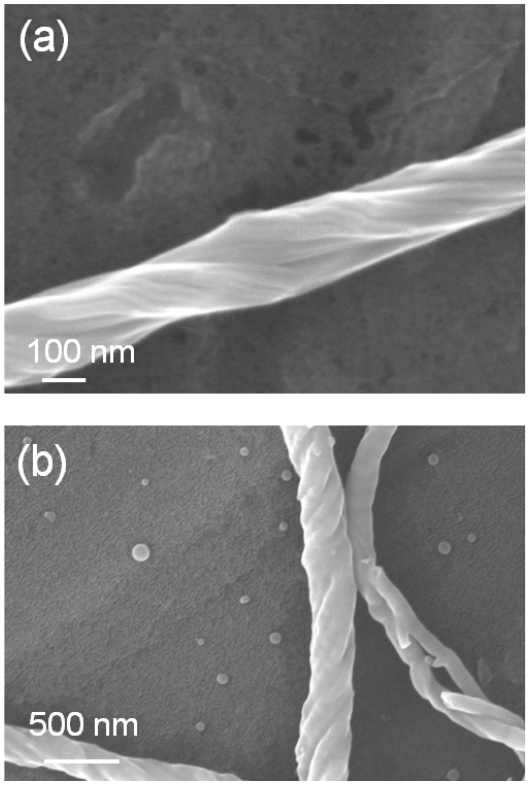

Figure 2. (a) L-glutathione から合成した錯体ナノヘリックスの SEM 画像(b) 右巻きヘリックス（R-$Cu_xAg_{2-x}S$ /C）の SEM 画

【参考文献】

[1] S. Che *et al.*, *Nature* **2004**, *429*, 281

[2] S. Liu *et al.*, *Nature Commun.* **2012**, *3*, 1215

[3] A. Sahu, L. J. Qi, M. S. Kang, D. N. Deng, D. J. Norris, *J. Am. Chem. Soc.* **2011**, *133*, 6509

3E08

RuCu 合金ナノ粒子の合成と物性

（京大院・理[1]，大分大・工[2]，九大院・工[3]，九大超顕微解析研究センター[4]）
○黄 博[1]，小林 浩和[1]，佐藤 勝俊[2]，山本 知一[3,4]，松村 晶[3,4]，永岡 勝俊[2]，北川 宏[1]

Keywords: Ruthenium; Copper; Nanoparticles; Alloy; Polyol Process Synthesis

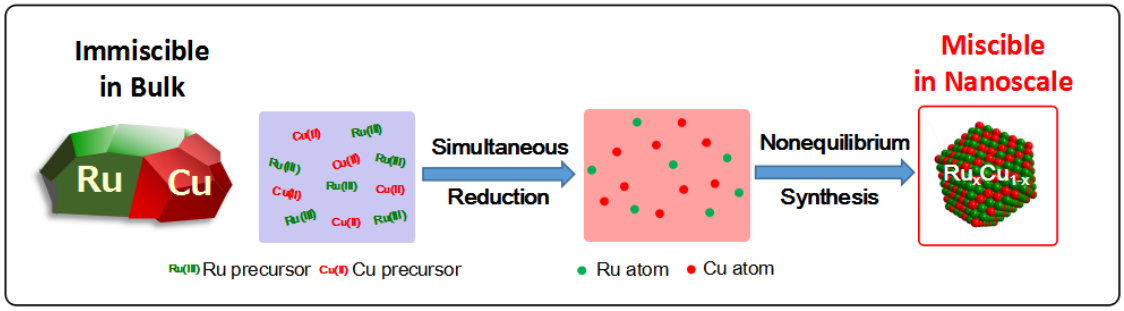

More attention has been paid to improving materials properties by means of alloying elements. In particular, the solid-solution type alloy has the advantage of being able to control the properties continuously by changing compositions and/or combinations of constituent elements. However, the majority of the bulk alloys are of the phase-separated type at ambient conditions, where constituent elements are immiscible with each other.

Ruthenium is major catalyst in many important industrial applications. On the other hand, copper is one of the cheapest metals with good catalytic performance. In the Ru-Cu bulk system,[1] these elements are immiscible, even in the liquid phase above 2400 °C; rather, the alloys form a segregated

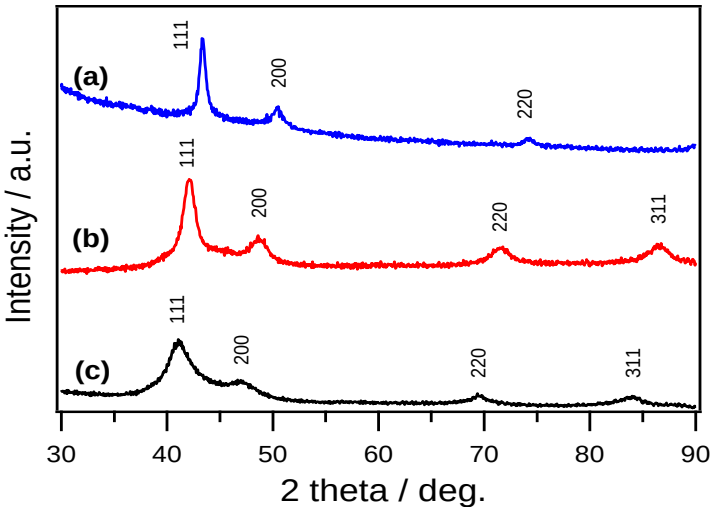

Fig.1. XRPD patterns of **(a)** Cu NPs, **(b)** RuCu NPs and **(c)** fcc Ru NPs.

domain structure. Therefore, RuCu solid-solution alloys have not been obtained so far.

Here, we first report on atomically mixed alloy nanoparticles (NPs) composed of Ru and Cu by means of polyol process. The RuCu alloy NPs were synthesized by a simultaneous reduction of Ru and Cu precursors in the presence of poly(N-vinyl-2-pyrrolidone). Diethylene glycol (DEG) was used as a solvent and a reducing agent. The mixture solution of the metal precursors was added into DEG solvent by syringe technique under inert condition. The reaction was performed under 230 °C for 10 min. The obtained RuCu NPs have been characterized by an X-ray powder diffraction (XRPD) and transmission electron microscope (TEM). From the XRPD pattern, RuCu NPs formed a face-centered cubic (fcc) structure as well as Ru and Cu monometallic nanoparticles. The diffraction peak positions of the RuCu NP were located between those of Ru and Cu NPs, suggesting the formation of atomic-level RuCu alloy. From scanning TEM image, the mean diameter of the RuCu NPs was estimated to be 7.8 ± 2.1 nm, and the overlay of energy dispersive spectroscopy (EDS) mappings demonstrated that Ru and Cu atoms are distributed over the whole particle.

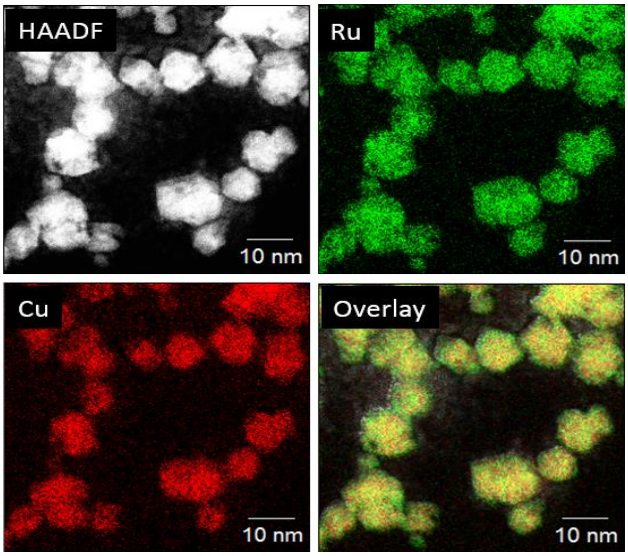

Fig.2. HAADF image and STEM-EDS mappings of RuCu NPs.

Reference

1. T.B. Massalski et al, Binary Alloy Phase Diagrams. Vol. I and II, ed. American Society of Metals,1986.

3E09

Ru-Fe ナノ合金アンモニア合成触媒の作製と触媒特性

（九州大学院・理 [1],九大 I2CNER[2],理研放射光科学総合研究セ [3])
○東﨑 康太 [1], 貞清 正彰 [1,2], 加藤 健一 [3], 山内 美穂 [1,2]

Preparations of Ru-Fe nanoalloy catalysts and their catalytic properties for ammonia synthesis

(Fac. Sci., Kyushu Univ.[1]; WPI-I2CNER, Kyushu Univ.[2]; RIKEN SPrin-8 Center[3])
○Kouta Touzaki[1], Masaaki Sadakiyo [2], Kenichi Kato [3], Miho Yamauchi[1,2]

【序論】アンモニアは、肥料の原料のみならず、CO_2 を排出しないクリーンなエネルギー媒体としても注目されている。現在、アンモニアは Fe 触媒を用いるハーバー・ボッシュ法により、工業的に生産されている。ハーバー・ボッシュ法によるアンモニア製造では、高温・高圧条件が必要であるため、世界の消費エネルギーの約 1%程度がアンモニア製造に由来すると言われている。環境保全の観点からは、エネルギー消費の少ない条件での製造法の開発が求められる。また、ハーバー・ボッシュ法で用いられる Fe 触媒は、最適化された条件では高活性であるが、生成した NH_3 に被毒されやすいという問題がある。他方、近年、低温・低圧条件でも活性を示す Ru 触媒が注目を集めている。しかしながら、Ru 触媒には H_2 に被毒され易いという弱点がある。本研究では、Fe と Ru の欠点を克服するため、両元素を固溶させた Ru-Fe 合金触媒を作製し、新たなアンモニア合成触媒を創製することを目的とする。

【実験】Ru-Fe ナノ合金粒子は含侵法により、Ru と Fe の割合を変えて合成した(Ru_xFe_{100-x}, x=100,90,80,70,60,50,40,30,20,10,5,0)。まず、金属源である Ru および Fe の錯体の溶液に MgO 担体を加え、アルゴン雰囲気下において室温で撹拌した。次に、前駆体を真空下、450℃で加熱することにより配位子および溶媒を除去して前駆体を作製した。さらに、5% H_2/Ar 気流下において前駆体の還元処理を行うことにより MgO 担持 Ru-Fe ナノ合金触媒（Ru_xFe_{100-x}/MgO）を作製した。Bruker 社製の D2 PHASER を用いて得られた試料の粉末 X 線回折(XRPD)測定を行った。JEOL 社製の JEM-ARM 200F を用いた走査透過型電子顕微鏡(STEM)観察および付属の JEOL 社製 STEM-EDS を用いた元素分析により、試料の構造・粒径等を評価した。また、MicrotracBEL 社製の流通式アンモニア反応装置（BEL-REA)を用いて、アンモニア合成触媒活性評価を行った。反応条件は 400 ℃, 1, 5, 10 気圧,

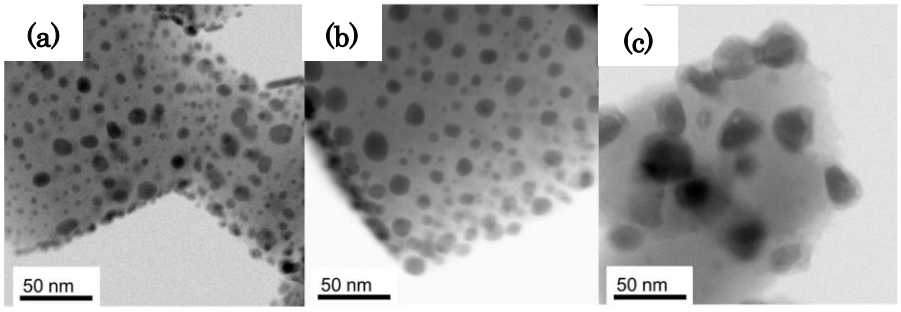

図 1 (a)Ru/MgO, (b)$Ru_{50}Fe_{50}$/MgO, (c)Fe/MgO の STEM 像.

H_2/N_2 = 3, 60 ccm とした。また、MicrotracBEL 社製の BELCAT-A-SP を用いて CO 化学吸着測定を行い触媒活性点を評価した。さらに、触媒表面の電子状態を明らかにするため、ULVAC-PHI 社製の Versa Probe PHI-5000 を使って X 線光電子分光測定(XPS)を行った。

【結果と考察】図 1 に、Ru/MgO, $Ru_{50}Fe_{50}$/MgO, Fe/MgO の STEM 像を示す。STEM 観察により、いずれの組成においても、ナノ粒子が MgO 担体上によく分散して存在していることが確認された。また、Fe 原子の割合が増えるにつれて粒径が大きくなる傾向があることがわかった。さらに、STEM-EDX を使った線分析では、組成比が Ru:Fe = 50:50 とわかり、Ru および Fe 原子が同一粒子内に均一に分布して存在し、固溶体型合金を形成していることが明らかとなった（図 2)。

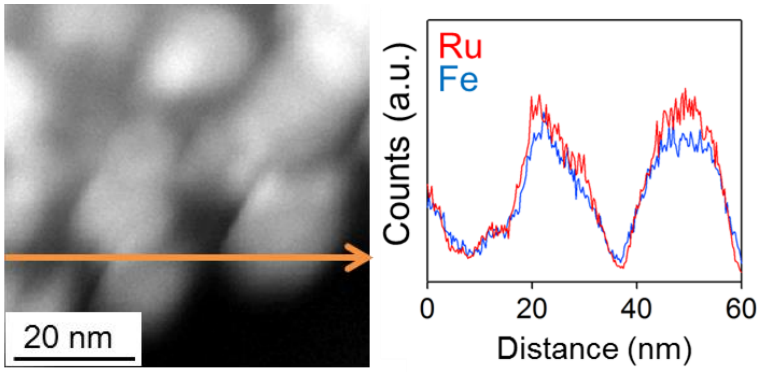

図 2 $Ru_{50}Fe_{50}$/MgO の線上での元素分布.

次に、Ru-Fe ナノ合金触媒のアンモニア合成触媒活性試験（1-10 気圧）の結果を図 3 に示す。1 気圧においては、Ru/MgO が最も高い活性を示した。他方、5 および 10 気圧においては、Ru-Fe ナノ合金が Ru 触媒より高い活性を示すことがわかった(図 3)。Fe/MgO はどの条件でも活性を示さなかった。Ru 原子あたりの触媒回転頻度を見積もると（図 4）、合金触媒は、単純な Ru 触媒より高い回転頻度を示すことがわかった。これは、Fe との合金化により活性点当たりの触媒活性が向上することを示唆するものである(図 4)。当日は、XPS スペクトルの結果と合わせて、触媒活性向上の原因についても議論を行う。

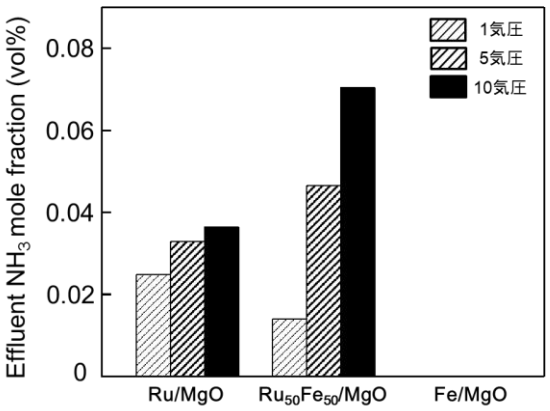

図 3 Ru/MgO, $Ru_{50}Fe_{50}$/MgO, Fe/MgO 上でのアンモニア生成量.

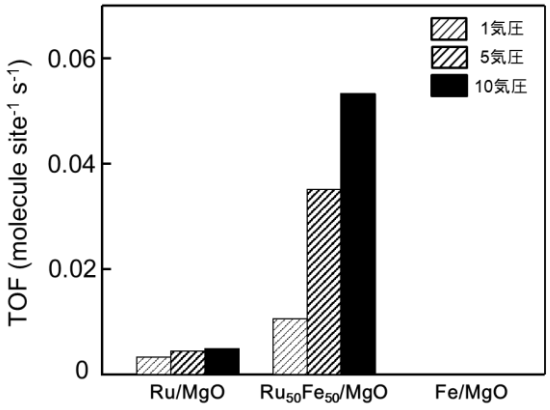

図 4 Ru/MgO, $Ru_{50}Fe_{50}$/MgO, Fe/MgO 上でのアンモニア合成触媒回転頻度.

【参考文献】 (1) M. Kitano et al., Nature. Chem. 2012, 4, 934-940.

3E10　セラミックのナノサイズ化による高親和的 CO_2 吸着能の発現

（千葉大学）　渡邊拓実，赤岩淳，星大樹，大場友則

High affinity to CO_2 adsorption through downsizing ceramic

(Chiba Univ.) Takumi Watanabe, Jun Akaiwa, Daiki Hoshi, Tomonori Ohba

【緒言】

二酸化炭素の排出削減は喫緊の課題となっている。二酸化炭素排出削減のために、吸着法による分離・除去は主要な技術の一つとなっており、そのための吸着材としてナノ空間を有した Zeolite や MOF、炭素材料は分子との強い相互作用によって吸着が促進されるため注目されている[1,2]。　また、強誘電セラミックも室温で自発分極を持ち、表面に電荷を有するため、分子との強い相互作用が期待されるが、表面積が極めて小さいために吸着量が少ない。よって、表面積の欠点さえ補うことができれば、セラミックも高い吸着能を示すと考えられる。　そこで本研究では代表的な強誘電セラミックの一つである $BaTiO_3$ をナノスケールで合成することで、表面積を増加させ、二酸化炭素吸着に対する高い吸着能の発現の可能性を模索した。

【実験】

Methanol, 2-methoxyethanol の混合溶液(3：2 v/v)を用いて、$[Ba(OEt)_2]$：$[Ti(O^iPr)_4]$ = 1：1 もしくは 2：1、$[Ti(O^iPr)_4]$ = 100 mM, 200 mM, 400mM になるように溶液を調製した。ここに、水蒸気を吸着した活性炭素繊維(ACF)をまぜて 400 K で 24 h 加熱し、$BaTiO_3$(Nano-BTO)を合成した[3]。ACF-BTO は 673 K 大気中(or N_2: O_2 = 8：2 雰囲気)で 48 時間加熱することで、ACF を低温酸化して除去した。同様に ACF ではなく水を混ぜて合成した $BaTiO_3$(Meso-BTO)と、$BaCO_3$ と TiO_2 を原料とした固相法により合成した $BaTiO_3$(Crystalline-BTO)を比較のため合成した。これらの $BaTiO_3$ に対して X 線回折(Rigaku / 40 kV, 40 mA / CuKα：λ = 0.1541 nm)・窒素吸着(Quantachrome：Autosorb / Pretreatment：423 K, 2 h / 77 K)・二酸化炭素吸着(Quantachrome：Autosorb / Pretreatment：423 K, 2 h / 273, 303, 333 K)測定を行った。

【結果・考察】

ACF のスリット径は約 1.4 nm であり、このナノ空間中で $BaTiO_3$ 合成を行った。ACF の二次元空間の制約により合成された $BaTiO_3$ は、サイズダウンとともに特異構造をもつことが先行研究からわかっており[3]、本研究でも同様の結果が得られた。窒素吸着等温線から比表面積を求め、そこから粒子の球形近似により平均粒子直径を求めた。比表面積が大きくなるにつれ、直径は小さくなり、Nano-BTO は 2～4 nm, Meso-BTO は 5～6 nm, Crystalline-BTO は 1000 nm 以上という結果が得られた。Fig. 1 に示した XRD から、Crystalline-BTO, Meso-BTO, Nano-BTO の順にピーク幅が広がっており、そこから Scherrer の式を用いて求められる結晶子径も Crystalline-BTO: 1200 nm, Meso-BTO: 9.3 nm, Nano-BTO: 2.7 nm と算出され、窒素吸着等温線から求められた平均直径同様小さくなった。

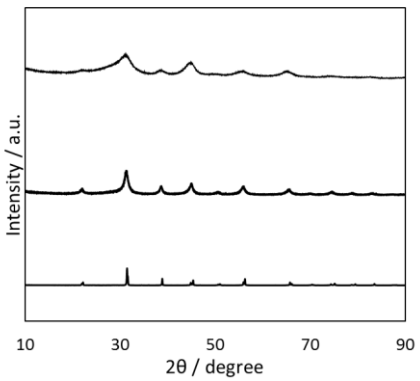

Fig. 1 各 $BaTiO_3$ の XRD パターン

窒素吸着量と同様に二酸化炭素吸着等温線から得られる吸着量は Nano-BTO > Meso-BTO > Crystalline-BTO の順となった。さらに各 $BaTiO_3$ の細孔容量あたりの二酸化炭素吸着量を他の代表的吸着媒と比較した(Fig. 2)。セラミックは本来、非多孔性材料であるため、一般的な Crystalline-BTO はほとんど二酸化炭素を吸着できない。一方、Meso-BTO、Nano-BTO

は一部のカーボン材料や有機金属錯体(MOF)のレコード値に匹敵する吸着能を示していることがわかった。また、333 K の高温においてさえ、高い吸着能を維持した。高い吸着能を定量的に表すために Clausius-Clapeyron 式から吸着熱を求め、二酸化炭素の凝固熱と比較した(Fig. 3)。Nano-BTO, Meso-BTO ともに二酸化炭素の凝固熱よりも高い吸着熱を示しており、おおまかに Nano > Meso-BTO となった。吸着量が増加すると、吸着媒－二酸化炭素間の相互作用が減少し、二酸化炭素－二酸化炭素間の相互作用が優先となるため、凝固熱に近づいた。このようにチタン酸バリウムに吸着された二酸化炭素は二酸化炭素の凝固による安定化よりも高い親和性がみられ、これは $BaTiO_3$ のナノサイズ化に伴う特異構造に起因しているのではないかと考えられる。今後は、Nano-BTO の特異構造を解明し、二酸化炭素に対する高い親和性との関係性を調べるとともに、この親和性を活かした効果的な二酸化炭素除去を目指す。

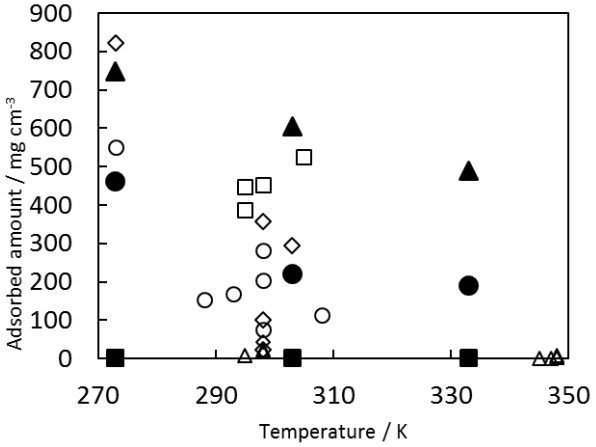

Fig. 2 各 $BaTiO_3$ と他吸着媒との二酸化炭素吸着量の比較。●: Nano-BTO, ▲: Meso-BTO, ■: Crystalline-BTO, ○: Carbon materials, □: Zeolite, ◇: MOF, and △: Meso porous silica.

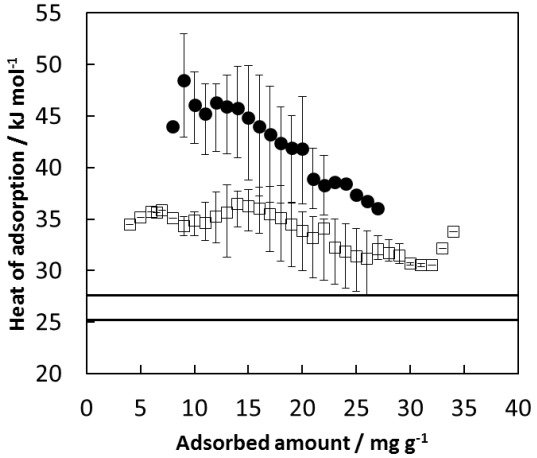

Fig. 3 各 $BaTiO_3$ の等量吸着熱。●: Nano-BTO and □: Meso-BTO.

【参考文献】

1) Yu *et al., AEROSOL AIR QUAL RES*, **2012**, *12*, 745
2) Deanna M. D'Alessandro *et al.*, *Angew. Chem.* Int. Ed., **2010**, *49*, 6058 – 6082
3) Ohba, T.; Ohyama, Y.; Kanoh, H., *RSD Adv.*, **2014**, *4*, 32647
4) Na, B. K.; Koo, K. K.; Eum, H. M.; Lee, H.; Song, H. K., *Korean J. Chem. Eng.* **2001**, *18*, 220–227.
5) Lu, C.; Bai, H.; Wu, B.; Su, F.; Hwang, J. F., *Energy Fuels* **2008**, *22*, 3050–3056.
6) Sircar, S.; Golden, T. C., *Ind. Eng. Chem. Res.* **1995**, *34*, 2881–2888.
7) Zhang, Z.; Zhang, W.; Chen, X.; Xia, Q.; Li, Z., *Sep.Sci. Technol.* **2010**, *45*, 710–719.
8) Su, F.; Lu, C.; Chen, W.; Bai, H.; Hwang, J. F., Sci.TotalEnviron., 2009, 407, 3017–3023.
9) Zhang, J.; Webley, P. A.; Xiao, P. *Energy Convers. Manage.* **2008**, *49*, 346–356.
10) Diaz,E.;Munoz,E.;Vega,A.;Ordonez,S., *Ind.Eng.Chem.Res.* **2008**, *47*, 412–418.
11) Bezerra, D. P.; Oliveira, R. S.; Vieira, R. S.; Cavalcante, C. L.; Azevedo, D. C. S., *Adsorption,* **2011**, *17*, 235–246
12) Calleja, G.; Jimenez, A.; Pau, J.; Dominguez, L.; Pbrez, P., *Gas. Sep. Purif.* **1994**, *8*, 247–256.
13) Choudhary,V.R.;Mayadevi,S.;Singh,A.P., *J. Chem. Soc., Faraday Trans.* **1995**, *91*, 2935–2944.
14) Harlick, P. J. E.; Tezel, F. H., Microporous Mesoporous Mater., **2004**, *76*, 71-79
15) Cavenati, S.; Grande, C. A.; Rodrigues, A. E., J. Chem. Eng. Data, **2004**, *49*, 1095–1101.